The Astrophysical Journal, 608:647–662, 2004 June 20

COSMOLOGICAL DENSITY DISTRIBUTION FUNCTION FROM THE ELLIPSOIDAL COLLAPSE MODEL IN REAL SPACE

Yasuhiro Ohta,[1] Issha Kayo,[1] and Atsushi Taruya[1,2]
Received 2003 October 23; accepted 2004 March 1

ABSTRACT

We calculate the one-point probability distribution function (PDF) for the cosmic density δ in the nonlinear regime of gravitational evolution. Under the local approximation that the evolution of cosmic fluid fields can be characterized by Lagrangian local dynamics with finite degrees of freedom, the analytic expressions of the PDF are derived taking into account the smoothing effect. The validity and the usefulness of the local approximation are then discussed, comparing those results with *N*-body simulations with Gaussian initial conditions. Adopting the ellipsoidal collapse model (ECM) and the spherical collapse model (SCM) for Lagrangian local dynamics, we found that the PDFs from the local approximation excellently match the simulation results in the case of a cold dark matter initial spectrum. As for the scale-free initial spectra given by $P(k) \propto k^n$, the *N*-body results suffer from spurious numerical effects, which prevent us from giving a detailed comparison. Nevertheless, for the quality of the *N*-body data, the model predictions based on the ECM and the SCM quantitatively agree with the *N*-body results in cases with spectral index $n < 0$. For index $n \geq 0$, the choice of Lagrangian local dynamics becomes crucial for an accurate prediction, and a more delicate modeling is required. However, we find that the model prediction based on the ECM provides a better approximation to the *N*-body results of cumulants and PDFs.

Subject headings: cosmology: theory — dark matter — galaxies: clusters: general — large-scale structure of universe — methods: analytical

1. INTRODUCTION

The probability distribution function (PDF) of the cosmological density fluctuation is a fundamental statistical quantity characterizing the large-scale structure of the universe. In the standard picture of cosmic structure formation based on the cold dark matter (CDM) scenario, the gravitational evolution of the dark matter distribution plays an essential role in the hierarchical nature of observed luminous distributions. Usually, the evolution of the dark matter distribution is believed to develop from a small initial fluctuation with a Gaussian random distribution. While the PDF of the density fluctuation retains a Gaussian shape in the linear regime, the deviation from a Gaussian distribution becomes significant in the nonlinear regime of gravitational evolution.

A number of studies in quantifying the non-Gaussian properties of the density field have been developed theoretically and observationally. From numerical and observational studies, a systematic analysis using a cosmological *N*-body simulation or the observed galaxy distribution yields various phenomenological prescriptions for the density PDF in the nonlinear regime (e.g., Saslaw & Hamilton 1984; Hamilton 1985; Gaztañaga & Yokoyama 1993; Ueda & Yokoyama 1996). Among them, the lognormal distribution has long been known to fit simulations quite accurately (e.g., Coles & Jones 1991; Coles et al. 1993; Bernardeau & Kofman 1995; Taylor & Watts 2000). Recently, Kayo et al. (2001) critically examined this issue using a high-resolution *N*-body simulation with Gaussian initial conditions and found that the accuracy of the lognormal model remains valid, irrespective of the nature of the initial spectra. The weak dependence of the initial spectra was later investigated using phenomenological models with a dark halo approach (Taruya et al. 2003).

On the other hand, in an analytical study, a perturbative construction of the PDFs was exploited by Bernardeau (1992, 1994a), employing a field-theoretical approach, and the predictions including the smoothing effect excellently match the *N*-body simulations in the weakly nonlinear regime. Beyond the perturbative prediction, however, no exact treatment is available, and a nonperturbative approximation or a phenomenological approach taking into account the empirical simulation results is necessary. Fosalba & Gaztañaga (1998a) and Scherrer & Gaztañaga (2001) proposed to use a spherical collapse model (SCM) as a nonperturbative approximation to predict the higher order moments and PDFs. In their treatment, one assumes that the Lagrangian dynamics of the local density field is simply described by an SCM. Although this approximation clearly misses the nonlocality of the gravity in the sense that the evolution of the local density field can be determined by one-to-one local mapping, the advantage of this treatment is that one can easily calculate the higher order corrections of the moments and PDFs. Furthermore, it turns out that the spherical collapse approximation exactly recovers the leading-order results of perturbation theory.

Recently, we generalized the idea of the spherical collapse approximation to a local approximation in which the evolution of the local density field is characterized by Lagrangian local dynamics with finite degrees of freedom (Ohta et al. 2003). As a demonstration, the PDFs were computed using the ellipsoidal collapse model (ECM). In the ECM the local density at a position is expressed as the multivariate function of initial parameters, i.e., the principal axes of the ellipsoid given at the same position. Thus, the relation between the initial and evolved density field cannot be described by one-to-one local mapping. As a consequence, the local approximation with an ECM successfully explains the stochastic nature seen in

[1] Department of Physics, School of Science, University of Tokyo, Tokyo 113-0033, Japan; ohta@utap.phys.s.u-tokyo.ac.jp, kayo@utap.phys.s.u-tokyo.ac.jp.
[2] Research Center for the Early Universe, School of Science, University of Tokyo, Tokyo 113-0033, Japan; ataruya@utap.phys.s.u-tokyo.ac.jp.

the simulation, i.e., the joint probability between the initial and evolved density fields, as has been reported by Kayo et al. (2001). In addition, the leading-order results from the ECM correctly reproduce those obtained from exact perturbation theory.

In the present paper we extend the previous study to a quantitative comparison between the local approximation and *N*-body simulations. Evaluating the PDF of the local density fields, taking into account the smoothing effect, we consider the validity and the limitation of the local approximation with SCMs and ECMs. The PDFs from the SCM were previously compared with *N*-body simulations in the case with a CDM power spectrum (Scherrer & Gaztañaga 2001). In this paper, taking into account the smoothing effect, *N*-body results with scale-free initial spectra as well as a CDM spectrum are compared.

This paper is organized as follows: In § 2 we start by reviewing the local approximation of one-point statistics developed by Ohta et al. (2003) and briefly show how to compute the PDF and the moments from the Lagrangian local collapse model. As representative models of Lagrangian local dynamics, the SCM and ECM are considered. Then, we consider the smoothing effect and discuss how to incorporate it into the model predictions. Based on this, the perturbative calculation of cumulants up to the two-loop order is presented, and the qualitative behaviors of the model prediction are discussed in § 3. In § 4 the validity and the usefulness of the local approximation for one-point statistics is investigated by comparing the PDFs and cumulants from the local collapse models with those obtained from *N*-body simulations. Finally, § 5 is devoted to discussion and conclusions.

2. ONE-POINT STATISTICS FROM THE LOCAL COLLAPSE MODEL

In many analytical works on the gravitational evolution of density distributions, the CDM distribution is often treated as a pressureless and nonrelativistic fluid. This treatment is not exact, but in a statistical sense, it would provide a better approximation if the scale of our interest were large enough, so that no shell crossing appeared in the smoothed density fields. Denoting the mass density and velocity field of the fluid by ρ and v, the evolution equations for the fluid in a homogeneous and isotropic background universe are expressed as

$$\frac{\partial \delta}{\partial t} + \frac{1}{a}\nabla\cdot[(1+\delta)\boldsymbol{v}] = 0, \tag{1}$$

$$\frac{\partial \boldsymbol{v}}{\partial t} + H\boldsymbol{v} + \frac{1}{a}(\boldsymbol{v}\cdot\nabla)\boldsymbol{v} = -\frac{1}{a}\nabla\phi, \tag{2}$$

where δ is the density fluctuation: $\delta \equiv (\rho - \rho_m)/\rho_m$. The quantity a is the scale factor of the universe, and H is the Hubble parameter, given by $H \equiv \dot{a}/a$. The gravitational potential ϕ is determined by the Poisson equation:

$$\nabla^2\phi = 4\pi G\rho_m a^2\delta. \tag{3}$$

Below, using the local approximation, we consider the one-point PDF of the density fluctuation δ and the higher order moments, taking into account the smoothing effect.

2.1. *Local Approximation*

As mentioned in § 1, the analytical treatment of the one-point PDF $P(\delta)$ governed by the fluid equations (1)–(3) is generally intractable because of the nonlinearity and nonlocality of the gravity. Beyond the perturbative prediction, a nonperturbative treatment should be exploited. The local approximation is one way to treat the one-point PDFs analytically, by reducing the Lagrangian dynamics of the fluid motion given by equations (1)–(3) to local dynamics with finite degrees of freedom. In this treatment, the time evolution of the local density field δ at a given position is determined by the local dynamics, with the initial condition given at the same position in Lagrangian coordinates. Thus, the solution of the local density field can be obtained by solving a couple of ordinary differential equations and can be expressed as a function of initial parameters $\boldsymbol{\lambda} = (\lambda_1, \lambda_2, \ldots, \lambda_n)$ given at a Lagrangian position and time, i.e., $\delta = f(\boldsymbol{\lambda}, t)$. In this paper we consider the SCM and ECM as representative examples of the Lagrangian local dynamics (see §§ 2.1.1 and 2.1.2). In this case the initial parameters of Lagrangian local dynamics correspond to the linearly extrapolated density fluctuation δ_l for the SCM and the principal axes of the initial homogeneous ellipsoid (λ_1, λ_2, λ_3) for the ECM.

Once provided the functional form of the local density, $f(\boldsymbol{\lambda}, t)$, the one-point PDF of the local density field $P(\delta; t)$ (in Eulerian space) can be analytically obtained. With a slight modification of the definition of the density fluctuation δ so as to satisfy the normalization condition and the zero mean of δ (Ohta et al. 2003), one has

$$P(\delta, t) = \frac{1}{1+\delta}\int \prod_{i=1}^{n} d\lambda_i\, P_I(\boldsymbol{\lambda})\delta_{\rm D}(\delta - g(\boldsymbol{\lambda}, t)), \tag{4}$$

where the function g is given by

$$\delta = g(\boldsymbol{\lambda}, t) \equiv N_{\rm E}[1 + f(\boldsymbol{\lambda}, t)] - 1,$$
$$N_{\rm E}(t) \equiv \int \prod_{i=1}^{n} d\lambda_i \frac{P_I(\boldsymbol{\lambda})}{1+f(\boldsymbol{\lambda}, t)}. \tag{5}$$

In equations (4) and (5), the function $P_I(\boldsymbol{\lambda})$ is the probability distribution of the initial parameters, which characterizes the randomness of the mass distribution. From equation (4) one also calculates the moments of the density fields:

$$\langle \delta^N \rangle \equiv \int \delta^N P(\delta, t)\, d\delta = \int \prod_{i=1}^{n} d\lambda_i \frac{g^N}{1+g} P_I(\boldsymbol{\lambda}). \tag{6}$$

Expressions (4)–(6) are the heart of the analytical treatment in the local approximation and are rigorously derived by considering the evolution equations for the one-point PDFs (Ohta et al. 2003).

2.1.1. *Spherical Collapse Model*

To calculate the function $f(\boldsymbol{\lambda}, t)$, let us first consider the SCM for the simple Lagrangian local dynamics. In the SCM the evolution of the local density at a given position in Lagrangian space is determined by the mass M inside a sphere of radius R collapsing via self gravity:

$$\frac{d^2R}{dt^2} = -\frac{GM}{R^2} + \frac{\Lambda}{3}R, \quad M = \frac{4\pi}{3}\bar{\rho}R^3 = \text{const}, \tag{7}$$

where Λ is the cosmological constant. The above equation is re-expressed in terms of the local density defined by $\delta = (aR_0/R)^3 - 1$:

$$\frac{d^2\delta}{dt^2} + 2H\frac{d\delta}{dt} - \frac{4}{3}\frac{1}{1+\delta}\left(\frac{d\delta}{dt}\right)^2 = \frac{3}{2}H^2\Omega_m(1+\delta)\delta, \tag{8}$$

where Ω_m is the density parameter given by $\Omega_m \equiv 8\pi G\rho_m/(3H^2)$. Note that the SCM can be regarded as the monopole approximation of the fluid equations neglecting the shear and vorticity (e.g., Fosalba & Gaztañaga 1998a), since one obtains the following from equations (1)–(3) with the help of the Lagrangian time derivative, $d/dt \equiv \partial/\partial t + \boldsymbol{v}/a \cdot \nabla$:

$$\frac{d^2\delta}{dt^2} + 2H\frac{d\delta}{dt} - \frac{4}{3}\frac{1}{1+\delta}\left(\frac{d\delta}{dt}\right)^2 = H^2(1+\delta)\left(\frac{3}{2}\Omega_m\delta + \sigma^{ij}\sigma_{ij} - \omega^{ij}\omega_{ij}\right), \quad (9)$$

$$\sigma_{ij} = \frac{1}{2aH}\left(\frac{\partial v_i}{\partial x_j} + \frac{\partial v_j}{\partial x_i} - \frac{2}{3}\nabla\cdot\boldsymbol{v}\delta_{ij}\right), \quad (10)$$

$$\omega_{ij} = \frac{1}{2aH}\left(\frac{\partial v_i}{\partial x_j} - \frac{\partial v_j}{\partial x_i}\right), \quad (11)$$

where σ_{ij} and ω_{ij} respectively denote the shear and vorticity tensors.

The exact solution of equation (7) is obtained in the case of an Einstein–de Sitter universe ($\Omega_m = 1,\ \Lambda = 0$) and is expressed as a function of the linearly extrapolated density fluctuation δ_l in parametric form:

$$\delta = \frac{9}{2}\frac{(\eta - \sin\eta)^2}{(1-\cos\eta)^3} - 1, \quad \delta_l = \frac{3}{5}\left[\frac{3}{4}(\eta - \sin\eta)\right]^{2/3} \quad (12)$$

for $\delta_l > 0$, and

$$\delta = \frac{9}{2}\frac{(\sinh\eta - \eta)^2}{(\cosh\eta - 1)^3} - 1, \quad \delta_l = -\frac{3}{5}\left[\frac{3}{4}(\sinh\eta - \eta)\right]^{2/3} \quad (13)$$

for $\delta_l < 0$. The relation between δ and δ_l in the above equation is fairly accurate even in the non–Einstein–de Sitter universe (e.g., Nakamura & Suto 1995; Fosalba & Gaztañaga 1998b). We extensively use equations (12) and (13) for later analysis. Note that in computing the density PDF, the linearly extrapolated density δ_l should be regarded as an initial parameter and treated as a random variable. Assuming Gaussian initial conditions, we have

$$P_I(\delta_l) = \frac{1}{\sqrt{2\pi}\sigma_l} e^{-(\delta_l/\sigma_l)^2/2}, \quad (14)$$

where the variable σ_l is the rms fluctuation of the linear density field, $\sigma_l = \langle\delta_l^2\rangle^{1/2}$.

2.1.2. *Ellipsoidal Collapse Model*

The ECM is an extension of the SCM, taking into account nonsphericity. In this model the dynamics of the local density is described by a self-gravitating uniform-density ellipsoid characterized by the half-length of the principal axes α_i ($i = 1, 2, 3$).

The local density of the ECM is given by

$$\delta = \frac{a^3}{\alpha_1\alpha_2\alpha_3} - 1. \quad (15)$$

According to Bond & Myers (1996), the evolution equations of the half-lengths of the axes become

$$\frac{d^2}{dt^2}\alpha_i = \frac{\Lambda}{3}\alpha_i - 4\pi G\rho_m\alpha_i\left(\frac{1+\delta}{3} + \frac{b_i}{2}\delta + \lambda_{\mathrm{ext},i}\right), \quad (16)$$

$$b_i = \alpha_1\alpha_2\alpha_3\int_0^\infty \frac{d\tau}{(\alpha_i^2+\tau)\prod_j(\alpha_j^2+\tau)^{1/2}} - \frac{2}{3}. \quad (17)$$

The quantity $\lambda_{\mathrm{ext},i}$ mimics the effect of the external tidal shear, which was introduced for consistency with the Zel'dovich approximation:

$$\lambda_{\mathrm{ext},i} = \begin{cases} \lambda_i - \dfrac{\lambda_1+\lambda_2+\lambda_3}{3}, & \text{linear external tide,} \\ \dfrac{5}{4}b_i, & \text{nonlinear external tide,} \end{cases} \quad (18)$$

where λ_i denotes the initial perturbation of the principal axis and evolves as $\lambda_i(t) = D(t)\lambda_i(t_0)$, with the variable D being the linear growth rate. Note that the inclusion of the external tidal term is necessary to reproduce the Zel'dovich approximation when we linearize the evolution equations.[3] In this paper both cases of the external tidal term are considered in order to reveal the model dependence of the prediction, but when comparing with N-body simulations, only the ECM results with the linear external tide are presented for brevity. In the presence of an external tide, the initial condition is specified by the Zel'dovich approximation. Identifying the variables λ_i with the initial parameters of α_i, we have

$$\alpha_i(t_0) = a(t_0)[1 - \lambda_i(t_0)], \quad (19)$$

$$\frac{d}{dt}\alpha_i(t_0) = \dot{a}(t_0)[1 - \lambda_i(t_0)] - a(t_0)\dot{\lambda}_i(t_0). \quad (20)$$

Note that the initial parameters λ_i are related to the linearly extrapolated density fluctuation δ_l by $\delta_l = \lambda_1 + \lambda_2 + \lambda_3$. Hence, the parameters λ_i should be treated as random variables. For Gaussian initial conditions, the distribution function of λ_i is analytically expressed as (Doroshkevich 1970)

$$P_I(\lambda_i) = \frac{675\sqrt{5}}{8\pi\sigma_l^6}\exp\left(-3\frac{I_1^2}{\sigma_l^2} + 15\frac{I_2}{2\sigma_l^2}\right) \times (\lambda_1-\lambda_2)(\lambda_2-\lambda_3)(\lambda_1-\lambda_3), \quad (21)$$

where we define $I_1 = \lambda_1 + \lambda_2 + \lambda_3$ and $I_2 = \lambda_1\lambda_2 + \lambda_2\lambda_3 + \lambda_3\lambda_1$.

Note that in contrast to the SCM, the ECM can be regarded as an approximation of the fluid equations taking into account the effect of tidal shear but neglecting the vorticity (Ohta et al. 2003). Equation (16) with equation (17) is re-expressed in terms of the local density δ (cf. eq. [9]):

$$\frac{d^2\delta}{dt^2} + 2H\frac{d\delta}{dt} - \frac{4}{3}\frac{1}{1+\delta}\left(\frac{d\delta}{dt}\right)^2 = H^2(1+\delta)\left(\frac{3}{2}\Omega_m\delta + \sigma^{ij}\sigma_{ij}\right), \quad (22)$$

$$\sigma_{ij} = \frac{1}{3H}\left(3\frac{\dot{\alpha}_i}{\alpha_i} - \frac{\dot{\alpha}_1}{\alpha_1} - \frac{\dot{\alpha}_2}{\alpha_2} - \frac{\dot{\alpha}_3}{\alpha_3}\right)\delta_{ij}. \quad (23)$$

2.2. *Smoothing Effect*

When we evaluate statistical quantities from N-body simulations, a smoothing procedure is often employed to remedy

[3] If this term is dropped, a consistent calculation with the initial distribution of eq. (21) is also impossible.

the discreteness of the particle data. In this sense the smoothing effect is crucial and should be incorporated into the theoretical prediction. In this paper we adopt top-hat smoothing, and the smoothed density PDFs are computed from both the local approximation and the N-body simulation:

$$\hat{\delta}(\boldsymbol{x};\ R) = \int d^3y\, \delta(\boldsymbol{y}) W_{\rm TH}(|\boldsymbol{y}-\boldsymbol{x}|;\ R), \tag{24}$$

$$W_{\rm TH}(r;\ R) = \begin{cases} \dfrac{3}{4}\pi R^3, & r < R, \\ 0, & \text{otherwise}, \end{cases} \tag{25}$$

where $W_{\rm TH}(r;\ R)$ is the top-hat smoothing kernel of radius R.

A systematic method for computing analytic PDFs taking into account the smoothing effect was first considered by Bernardeau (1994a), based on perturbation theory. Later, his method was extended to the nonperturbative calculation of the PDF using the SCM (Fosalba & Gaztañaga 1998a). We briefly review the method by Fosalba & Gaztañaga (1998a).

First, notice the fact that in the case of top-hat smoothing, the leading-order results of cumulants for the local density field are not affected by smoothing in Lagrangian space (Bernardeau 1994a). Extrapolating this result to the nonperturbative approximation with the SCM, one can approximate the evolved local density with top-hat smoothing by

$$\hat{\delta} \approx f(\delta_{l,\rm L}), \tag{26}$$

where $\hat{\delta}$ is the smoothed density and $\delta_{l,\rm L}$ is the linear density fluctuation in Lagrangian space. To relate the quantity $\delta_{l,\rm L}$ to that in Eulerian space, $\delta_{l,\rm E}$, we recall the fact that the radius R defined in Eulerian space roughly corresponds to the radius $R(1+\hat{\delta})^{1/3}$ in Lagrangian space. Thus, we have

$$\frac{\delta_{l,\rm E}}{\sigma_l(R)} = \frac{\delta_{l,\rm L}}{\sigma_l\left[R\left(1+\hat{\delta}\right)^{1/3}\right]}. \tag{27}$$

Substituting equation (27) into equation (26) and identifying the linear fluctuation $\delta_{l,\rm E}$ with the smoothed linear fluctuation $\hat{\delta}_l$, the relation between $\hat{\delta}$ and $\hat{\delta}_l$ becomes

$$\hat{\delta} = \hat{f}\left(\hat{\delta}_l\right) \approx f\left(\frac{\sigma_l\left[R\left(1+\hat{\delta}\right)^{1/3}\right]}{\sigma_l(R)}\hat{\delta}_l\right). \tag{28}$$

The above relation can be further simplified with the running index γ, defined as $\gamma \equiv d\log\sigma_l^2/d\log R$:

$$\hat{f}\left(\hat{\delta}_l\right) = f\left(\left[1+\hat{f}\left(\hat{\delta}_l\right)\right]^{\gamma/6}\hat{\delta}_l\right), \quad \gamma = \frac{d\log\sigma_l^2}{d\log R} = -(n+3), \tag{29}$$

where n is the index of the initial power spectrum, $P(k) \propto k^n$. Notice that the above expression is still valid in the non–power-law cases of the initial power spectrum. The remarkable feature in relation (28) or (29) is that the leading-order result of the cumulants obtained from the perturbation theory is exactly recovered by the local approximation with the SCM.

Owing to this noticeable fact, we extend the result of equation (29) to the local approximation with the ECM. In this case the smoothed density field is related to the top-hat–filtered principal axis $\hat{\lambda}_i$ by

$$\hat{f}\left(\hat{\boldsymbol{\lambda}},\ t\right) = f\left(\left[1+\hat{f}\left(\hat{\boldsymbol{\lambda}},\ t\right)\right]^{\gamma/6}\hat{\boldsymbol{\lambda}},\ t\right). \tag{30}$$

Adopting this form, the PDF in equation (4) becomes

$$P\left(\hat{\delta};\ R\right) = \frac{1}{1+\hat{\delta}}\int\prod_{i=1}^{3} d\hat{\lambda}_i P_I\left(\hat{\boldsymbol{\lambda}}\right)\delta_{\rm D}\left(\hat{\delta}-\hat{g}\left(\hat{\boldsymbol{\lambda}},\ t\right)\right), \tag{31}$$

with $\hat{g}(\hat{\boldsymbol{\lambda}},\ t)$ being

$$\hat{g}\left(\hat{\boldsymbol{\lambda}},\ t\right) = \hat{N}_{\rm E}\left[1+\hat{f}\left(\hat{\boldsymbol{\lambda}}\right),\ t\right] - 1,$$
$$\hat{N}_{\rm E}(t) = \int\prod_i d\hat{\lambda}_i\, \frac{P_I\left(\hat{\boldsymbol{\lambda}}\right)}{1+\hat{f}\left(\hat{\boldsymbol{\lambda}},\ t\right)}. \tag{32}$$

The above equations seem difficult to evaluate because of the implicit relation of the functions $\hat{f}$ and $\hat{\boldsymbol{\lambda}}$. However, this apparent difficulty can be eliminated by introducing the following variables:

$$\lambda_i' = \left[1+\hat{f}\left(\hat{\boldsymbol{\lambda}},\ t\right)\right]^{\gamma/6}\hat{\lambda}_i. \tag{33}$$

Then equation (31) becomes

$$P\left(\hat{\delta};\ R\right) = \frac{1}{1+\hat{\delta}}\int\prod_{i=1}^{3} d\lambda_i' P_I\left\{\left[1+f(\boldsymbol{\lambda}',\ t)\right]^{-\gamma/6}\boldsymbol{\lambda}'\right\} \times \delta_{\rm D}\left[\hat{\delta}-\hat{g}(\boldsymbol{\lambda}',\ t)\right]\left|\frac{\partial\hat{\lambda}_j}{\partial\lambda_k'}\right|, \tag{34}$$

where the quantities $\hat{g}$ and $\hat{N}_{\rm E}$ can be recast as

$$\hat{g}(\boldsymbol{\lambda}',\ t) = \hat{N}_{\rm E}[1+f(\boldsymbol{\lambda}',\ t)] - 1,$$
$$\hat{N}_{\rm E}(t) = \int\prod_i d\lambda_i'\, \frac{P_I\left\{\left[1+f(\boldsymbol{\lambda}',\ t)\right]^{-\gamma/6}\boldsymbol{\lambda}'\right\}}{1+f(\boldsymbol{\lambda}',\ t)}\left|\frac{\partial\hat{\lambda}_j}{\partial\lambda_k'}\right|. \tag{35}$$

In addition, the Jacobian $|\partial\hat{\lambda}_j/\partial\lambda_k'|$ is calculated using the relation $\hat{\lambda}_i = [1+f(\boldsymbol{\lambda},\ t)]^{-\gamma/6}\lambda_i'$ as

$$\left|\frac{\partial\hat{\lambda}_j}{\partial\lambda_k'}\right| = [1+f(\boldsymbol{\lambda}',\ t)]^{-\gamma/2}\left(1-\frac{\gamma}{6}\frac{1}{1+f}\sum_{i=1}^{3}\lambda_i'\frac{\partial f}{\partial\lambda_i'}\right). \tag{36}$$

Note that the term $-1/(1+f)\sum_{i=1}^{3}\lambda_i'(\partial f/\partial\lambda_i')$ is related to the velocity divergence and is expressed as $\theta = \sum_i \dot{\alpha}_i/(H\alpha_i) - 3$ in the case of an Einstein–de Sitter universe. Thus, provided the solution of the equations for the ECM (eqs. [15]–[17]), the smoothed density PDF can be numerically evaluated by substituting the solution $f(\boldsymbol{\lambda},\ t)$ into the above equations. Similarly, the higher order moments of the local density become

$$\left\langle\hat{\delta}^N\right\rangle = \int\hat{\delta}^N P\left(\hat{\delta};\ R\right)d\delta = \int\prod_{i=1}^{3} d\lambda_i'\, \frac{\hat{g}^N}{1+\hat{g}}P_I\left[(1+f)^{-\gamma/6}\boldsymbol{\lambda}'\right]\left|\frac{\partial\hat{\lambda}_j}{\partial\lambda_k'}\right|. \tag{37}$$

In what follows, we simply denote the smoothed density field $\hat{\delta}$ by δ.

3. PERTURBATION THEORY IN THE ELLIPSOIDAL COLLAPSE MODEL

Before comparing the theoretical models with N-body simulations, it is useful to examine the perturbative analysis of

the local collapse models. In this section, based on the ECM, we present the perturbative calculation of the cumulants of the density field. The differences between the model predictions, as well as the qualitative behaviors, are also discussed in § 3.3.

Here and in what follows, we treat the evolution of the local density in an Einstein–de Sitter universe. In this case the linear growth rate D is simply proportional to the scale factor a. Let us denote the half-length of the principal axis α_i by

$$\alpha_i(t) = a(t)[1 - \zeta_i(a(t))]. \tag{38}$$

Then, regarding the scale factor a as time-variable, equation (16) is transformed to

$$a^2 \frac{d^2\zeta_i}{da^2} + \frac{3}{2} a \frac{d\zeta_i}{da} = \frac{3}{2}(1-\zeta_i)\left(\frac{1}{3}\delta + \frac{1}{2} b_i \delta + \lambda_{\mathrm{ext},i}\right). \tag{39}$$

In terms of the variable ζ_i, the quantities b_i and δ are expressed as

$$b_i = (1-\zeta_1)(1-\zeta_2)(1-\zeta_3) \times \int_0^\infty \frac{d\tau}{\left[(1-\zeta_i)^2+\tau\right]\prod_j \left[(1-\zeta_j)^2+\tau\right]^{1/2}} - \frac{2}{3} \tag{40}$$

$$\equiv \frac{4}{15}[3\zeta_i - (\zeta_1+\zeta_2+\zeta_3)] + \tilde{b}_i, \tag{41}$$

$$\delta \equiv \zeta_1 + \zeta_2 + \zeta_3 + \Delta. \tag{42}$$

Note that both the quantities $\tilde{b}_i$ and Δ are $O(\zeta^2)$.

Below, we separately give the perturbation results in the ECM with a nonlinear external tide and with a linear external tide. Note that the leading-order results for the cumulants in each model exactly coincide with each other and reproduce those of exact perturbation theory (e.g., Bernardeau 1994a, 1994b).

3.1. *Ellipsoidal Collapse Model with a Nonlinear External Tide*

In the case of the model with a nonlinear external tide, the quantity $\lambda_{\mathrm{ext},i}$ is given by $(5/4)b_i$, and the right-hand side of equation (39) becomes $3\zeta_i/2 + O(\zeta^2)$. Then we have

$$a^2 \frac{d^2\zeta_i}{da^2} + \frac{3}{2} a \frac{d\zeta_i}{da} - \frac{3}{2}\zeta_i = \frac{1}{2}(\Delta - \delta\zeta_i) + \frac{3}{4}(1-\zeta_i)b_i\delta + \frac{15}{8}\left(\tilde{b}_i - \zeta_i b_i\right) = O\left(\zeta^2\right). \tag{43}$$

This equation can be perturbatively solved by substituting the series expansion $\zeta_i = \sum_{j=0} \xi_i^{(j)} a^j$ into the above equation. Under the initial condition (19), one formally obtains the expression of the coefficient $\xi_i^{(j)}$ as

$$\xi_i^{(1)} = \lambda_i(t_0), \tag{44}$$

$$\xi_i^{(j)} = \frac{1}{(2j+3)(j-1)j!}\frac{d^j}{da^j}\left[\Delta - \delta\zeta_i + \frac{3}{2}(1-\zeta_i)b_i\delta + \frac{15}{4}\left(\tilde{b}_i - \zeta_i b_i\right)\right]\Bigg|_{a=0}, \quad j > 1, \tag{45}$$

where we have only considered the growing mode of the solutions. Note that the coefficient $\xi_i^{(j)}$ is a variable of $O(\lambda^j)$.

Based on the result in equation (45), the perturbative expansion for the evolved density, $\delta = \sum_i \delta^{(i)}$, can be constructed from the relations (15), (38), and (40). The results up to the seventh order become

$$\delta^{(1)} = \delta_l, \tag{46}$$

$$\delta^{(2)} = \frac{17}{21}\delta_l^2 + \frac{4}{21}J_1, \tag{47}$$

$$\delta^{(3)} = \frac{341}{567}\delta_l^3 + \frac{338}{945}\delta_l J_1 + \frac{92}{3969}J_2, \tag{48}$$

$$\delta^{(4)} = \frac{55805}{130977}\delta_l^4 + \frac{485288}{1091475}\delta_l^2 J_1 + \frac{234088}{4584195}\delta_l J_2 + \frac{429728}{10696455}J_1^2, \tag{49}$$

$$\delta^{(5)} = \frac{213662}{729729}\delta_l^5 + \frac{292398464}{638512875}\delta_l^3 J_1 + \frac{64182728}{893918025}\delta_l^2 J_2 + \frac{6541246}{59594535}\delta_l J_1^2 + \frac{828974992}{96364363095}J_1 J_2, \tag{50}$$

$$\delta^{(6)} = \frac{21129781}{107270163}\delta_l^6 + \frac{15739030628}{37246584375}\delta_l^4 J_1 + \frac{38380501904}{469306963125}\delta_l^3 J_2 + \frac{334168450808}{1825082634375}\delta_l^2 J_1^2 + \frac{250313183728}{9368757523125}\delta_l J_1 J_2 + \frac{63778345006048}{7673012411439375}J_1^3 + \frac{2272657750768}{4603807446863625}J_2^2, \tag{51}$$

$$\delta^{(7)} = \frac{83411812}{639441621}\delta_l^7 + \frac{42267062029204}{116564878828125}\delta_l^5 J_1 + \frac{63224677073056}{769328200265625}\delta_l^4 J_2 + \frac{3019799334120902}{12565693937671875}\delta_l^3 J_1^2 + \frac{9581060236980928}{193511686640146875}\delta_l^2 J_1 J_2 + \frac{13515215809239748}{451527268827009375}\delta_l J_1^3 + \frac{276922264619192}{162549816777723375}\delta_l J_2^2 + \frac{9155185965341512}{3521912696850673125}J_1^2 J_2, \tag{52}$$

where δ_l denotes the linear fluctuation, given by $\delta_l = \lambda_1 + \lambda_2 + \lambda_3$. Here we introduced the quantities $J_1 \equiv x^2 + xy + y^2$ and $J_2 \equiv (x-y)(2x+y)(x+2y)$, with the variables x and y being $x = \lambda_1 - \lambda_2$ and $y = \lambda_2 - \lambda_3$, respectively.

Once provided the perturbative solution for the nonsmoothed density field, cumulants for the smoothed density are calculated as follows: From the perturbative inversion of relation (30), the smoothed density $\hat{\delta}$ is obtained, and the normalization factor $\hat{N}_{\mathrm{E}}$ is first calculated by substituting this into definition (32). Using the probability distribution of the initial parameter in equation (21), the resulting expression becomes

$$N_{\mathrm{E}} = 1 - \frac{1}{6}\gamma\sigma_l^2 + \left(\frac{10844}{848925} - \frac{79}{4410}\gamma - \frac{31}{378}\gamma^2 - \frac{1}{27}\gamma^3\right)\sigma_l^4 + \left(\frac{3891599696}{511023137625} - \frac{1248901}{278107830}\gamma - \frac{47093}{415800}\gamma^2 - \frac{62341}{317520}\gamma^3 - \frac{19}{168}\gamma^4 - \frac{1}{48}\gamma^5\right)\sigma_l^6 \tag{53}$$

up to $O(\sigma_l^6)$. Then the moments for the smoothed density $\langle\hat{\delta}^N\rangle$ are evaluated from the relation

$$\langle\hat{\delta}^N\rangle = \int \prod_i d\lambda_i \frac{\hat{g}^N}{1+\hat{g}} P_I(\boldsymbol{\lambda})$$

(cf. eq. [6]). Finally, the perturbative correction for the variance $\sigma^2 = \langle\hat{\delta}^2\rangle$, the skewness $S_3 = \langle\hat{\delta}^3\rangle/\sigma^4$, and the kurtosis $S_4 = (\langle\hat{\delta}^4\rangle - 3\sigma^4)/\sigma^6$ are obtained and can be summarized as series expansions of σ_l^2:

$$\sigma^2 = \sigma_l^2 + s_{2,4}\sigma_l^4 + s_{2,6}\sigma_l^6 + s_{2,8}\sigma_l^8 + \ldots, \tag{54}$$

$$S_3 = S_{3,0} + S_{3,2}\sigma_l^2 + S_{3,4}\sigma_l^4 + \ldots, \tag{55}$$

$$S_4 = S_{4,0} + S_{4,2}\sigma_l^2 + S_{4,4}\sigma_l^4 + \ldots. \tag{56}$$

The resulting expressions for the coefficients $s_{2,i}$, $S_{3,i}$ and $S_{4,i}$ become

$$s_{2,4} = \frac{439}{245} + \frac{167}{126}\gamma + \frac{11}{36}\gamma^2, \tag{57}$$

$$s_{2,6} = \frac{3143785639}{695269575} + \frac{15856223}{2037420}\gamma + \frac{55273}{10584}\gamma^2 + \frac{1835}{1134}\gamma^3 + \frac{127}{648}\gamma^4, \tag{58}$$

$$s_{2,8} = \frac{7932609222047169799}{537532462889296875} + \frac{2321384486861437}{54752479031250}\gamma + \frac{1062497682871}{20858087250}\gamma^2 + \frac{16268385923}{495093060}\gamma^3 + \frac{61875775}{5143824}\gamma^4 + \frac{13831}{5832}\gamma^5 + \frac{6877}{34992}\gamma^6 \tag{59}$$

for the variance,

$$S_{3,0} = \frac{34}{7} + \gamma, \tag{60}$$

$$S_{3,2} = \frac{1041064}{101871} + \frac{21946}{2205}\gamma + \frac{415}{126}\gamma^2 + \frac{10}{27}\gamma^3, \tag{61}$$

$$S_{3,4} = \frac{161751288183332}{3041804390625} + \frac{363349617641}{3476347875}\gamma + \frac{415283963}{5093550}\gamma^2 + \frac{11299781}{357210}\gamma^3 + \frac{2975}{486}\gamma^4 + \frac{1841}{3888}\gamma^5 \tag{62}$$

for the skewness, and

$$S_{4,0} = \frac{60712}{1323} + \frac{62}{3}\gamma + \frac{7}{3}\gamma^2, \tag{63}$$

$$S_{4,2} = \frac{941370178286}{3476347875} + \frac{1518808496}{4584195}\gamma + \frac{18161033}{119070}\gamma^2 + \frac{3935}{126}\gamma^3 + \frac{1549}{648}\gamma^4, \tag{64}$$

$$S_{4,4} = \frac{30144942925392628918}{13782883663828125} + \frac{129392230965050887}{27376239515625}\gamma + \frac{397096017904379}{93861392625}\gamma^2 + \frac{30126971437}{15002820}\gamma^3 + \frac{1142621801}{2143260}\gamma^4 + \frac{6127195}{81648}\gamma^5 + \frac{102005}{23328}\gamma^6 \tag{65}$$

for the kurtosis.

3.2. *Ellipsoidal Collapse Model with a Linear External Tide*

For the perturbative solution in the model with a linear external tide, the calculation is slightly reduced if we introduce the quantities $A = \zeta_1 + \zeta_2 + \zeta_3$, $B = \zeta_1 - \zeta_2$, and $C = \zeta_2 - \zeta_3$. Recalling the fact that the external tidal term becomes $\lambda_{\mathrm{ext},i} = \lambda_i - (\lambda_1 + \lambda_2 + \lambda_3)/3$, the evolution equation (39) is rewritten as

$$a^2\frac{d^2A}{da^2} + \frac{3}{2}a\frac{dA}{da} - \frac{3}{2}A = \frac{3}{2}\Delta - \frac{1}{2}\delta A - \frac{3}{4}\sum_{i=1}^{3}\zeta_i\left(\delta b_i + 2\lambda_{\mathrm{ext},i}\right), \tag{66}$$

$$a^2\frac{d^2B}{da^2} + \frac{3}{2}a\frac{dB}{da} - \frac{3}{2}(\lambda_1 - \lambda_2) = \frac{3}{4}\delta[(1-\zeta_1)b_1 - (1-\zeta_2)b_2] - \frac{1}{2}\delta B - \frac{3}{2}\left(\zeta_1\lambda_{\mathrm{ext},1} - \zeta_2\lambda_{\mathrm{ext},2}\right), \tag{67}$$

$$a^2\frac{d^2C}{da^2} + \frac{3}{2}a\frac{dC}{da} - \frac{3}{2}(\lambda_2 - \lambda_3) = \frac{3}{4}\delta[(1-\zeta_2)b_2 - (1-\zeta_3)b_3] - \frac{1}{2}\delta C - \frac{3}{2}\left(\zeta_2\lambda_{\mathrm{ext},2} - \zeta_3\lambda_{\mathrm{ext},3}\right). \tag{68}$$

Note also that the right-hand sides of equations (66)–(68) are of $O(\lambda^2)$.

Similar to the procedure in § 3.1, the perturbative expansion for the density δ is constructed from the perturbative solutions of A, B, and C. After a tedious but straightforward calculation, the perturbative solutions up to the seventh order become

$$\delta^{(1)} = \delta_l, \tag{69}$$

$$\delta^{(2)} = \frac{17}{21}\delta_l^2 + \frac{4}{21}J_1, \tag{70}$$

$$\delta^{(3)} = \frac{341}{567}\delta_l^3 + \frac{1538}{4725}\delta_l J_1 + \frac{4}{405}J_2, \tag{71}$$

$$\delta^{(4)} = \frac{55805}{130977}\delta_l^4 + \frac{952144}{2480625}\delta_l^2 J_1 + \frac{345088}{16372125}\delta_l J_2 + \frac{12368}{363825}J_1^2, \tag{72}$$

$$\delta^{(5)} = \frac{213662}{729729}\delta_l^5 + \frac{237342074}{621928125}\delta_l^3 J_1 + \frac{93363344}{3192564375}\delta_l^2 J_2 + \frac{52865818}{638512875}\delta_l J_1^2 + \frac{135052}{34827975}J_1 J_2, \tag{73}$$

$$\delta^{(6)} = \frac{21129781}{107270163}\delta_l^6 + \frac{73816004896012}{215099024765625}\delta_l^4 J_1 + \frac{29134959410408}{879950555859375}\delta_l^3 J_2 + \frac{45534497984}{355535578125}\delta_l^2 J_1^2 + \frac{1416570594232}{129059414859375}\delta_l J_1 J_2 + \frac{797014912}{132368630625}J_1^3 + \frac{162352}{1578740625}J_2^2, \tag{74}$$

$$\delta^{(7)} = \frac{83411812}{639441621}\delta_l^7 + \frac{24700151148166244}{85566392051765625}\delta_l^5 J_1 + \frac{49159400006961656}{1480956785511328125}\delta_l^4 J_2 + \frac{18569055254261594}{116681443706953125}\delta_l^3 J_1^2 + \frac{13101172588796}{684531136414125}\delta_l^2 J_1 J_2 + \frac{9323215177292}{488950811724375}\delta_l J_1^3 + \frac{1452480606736}{4400557305519375}\delta_l J_2^2 + \frac{11003633175272}{10267967046211875}J_1^2 J_2. \tag{75}$$

TABLE 1

Coefficients of Perturbative Correction for the Cumulants of the Density Field

n	$s_{2,4}$	$s_{2,6}$	$s_{2,8}$	$S_{3,2}$	$S_{3,4}$	$S_{4,2}$	$S_{4,4}$
Nonlinear External Tide							
−3	1.79	4.52	14.8	10.2	53.2	271	2.19×10^3
−2	0.772	0.539	0.294	3.19	4.20	63.2	146
−1	0.363	0.0364	-7.50×10^{-4}	0.525	−0.0169	6.67	0.614
0	0.566	0.360	0.158	0.00379	0.0646	−0.0227	0.364
Linear External Tide							
−3	1.73	4.20	13.3	10.2	51.7	269	2.14×10^3
−2	0.708	0.442	0.199	3.19	3.98	63.1	141
−1	0.299	−0.0202	−0.0113	0.587	0.0119	7.32	1.16
0	0.501	0.165	−0.235	0.130	0.246	0.651	1.41

The normalization factor of the PDF is

$$N_{\rm E} = 1 - \frac{1}{6}\gamma\sigma_l^2 + \left(\frac{69668}{3898125} + \frac{701}{198450}\gamma - \frac{31}{378}\gamma^2 - \frac{1}{27}\gamma^4\right)\sigma_l^4 + \left(\frac{5033872069084}{645297074296875} + \frac{3873942169}{223479506250}\gamma - \frac{38616157}{509355000}\gamma^2 - \frac{286169}{1587600}\gamma^3 - \frac{19}{168}\gamma^4 - \frac{1}{48}\gamma^5\right)\sigma_l^6. \quad (76)$$

Then the coefficients of the perturbative corrections for cumulants become

$$s_{2,4} = \frac{57137}{33075} + \frac{167}{126}\gamma + \frac{11}{36}\gamma^2, \quad (77)$$

$$s_{2,6} = \frac{469828713881}{111739753125} + \frac{17130160379}{2292097500}\gamma + \frac{488945}{95256}\gamma^2 + \frac{1835}{1134}\gamma^3 + \frac{127}{648}\gamma^4, \quad (78)$$

$$s_{2,8} = \frac{996244294855051546571}{74870593045294921875} + \frac{152613969392185373}{3871782445781250}\gamma + \frac{683964582869801}{14079208893750}\gamma^2 + \frac{1980638022487}{61886632500}\gamma^3 + \frac{306289019}{25719120}\gamma^4 + \frac{13831}{5832}\gamma^5 + \frac{6877}{34992}\gamma^6 \quad (79)$$

for the variance,

$$S_{3,0} = \frac{34}{7} + \gamma, \quad (80)$$

$$S_{3,2} = \frac{646404856}{63669375} + \frac{327062}{33075}\gamma + \frac{415}{126}\gamma^2 + \frac{10}{27}\gamma^3, \quad (81)$$

$$S_{3,4} = \frac{77881923244216108}{1505693173359375} + \frac{80186055186641}{782178271875}\gamma + \frac{2052918391}{25467750}\gamma^2 + \frac{56239289}{1786050}\gamma^3 + \frac{2975}{486}\gamma^4 + \frac{1841}{3888}\gamma^5 \quad (82)$$

for the skewness, and

$$S_{4,0} = \frac{60712}{1323} + \frac{62}{3}\gamma + \frac{7}{3}\gamma^2, \quad (83)$$

$$S_{4,2} = \frac{210688932175742}{782178271875} + \frac{188859083824}{573024375}\gamma + \frac{90600877}{595350}\gamma^2 + \frac{3935}{126}\gamma^3 + \frac{1549}{648}\gamma^4, \quad (84)$$

$$S_{4,4} = \frac{10213314999275942085 5618}{47644922847005859375} + \frac{7007053550215029257}{1505693173359375}\gamma + \frac{29469590927547677}{7039604446875}\gamma^2 + \frac{13726819977457}{6876292500}\gamma^3 + \frac{5700735749}{10716300}\gamma^4 + \frac{6127195}{81648}\gamma^5 + \frac{102005}{23328}\gamma^6 \quad (85)$$

for the kurtosis.

3.3. *Differences between Model Predictions*

To understand both the qualitative and the quantitative behaviors of the above two predictions, we here briefly discuss the systematic dependence of the perturbative results. Table 1 summarizes the numerical values of the coefficients, $s_{2,i}$ up to the three-loop order and $S_{3,i}$ and $S_{4,i}$ up to the two-loop order for each model with various spectral indexes. Using these results, we plot the cumulants up to the two-loop order in Figure 1, in which the cumulants are normalized by the leading-order results for σ_l^2, $S_{3,0}$, and $S_{4,0}$ (*top to bottom*) and are depicted as functions of linear variance σ_l. The results from the SCM (*short-dashed lines*) are essentially the same results as those obtained by Fosalba & Gaztañaga (1998a). Note that the leading-order results for the cumulants in all model predictions rigorously coincide with those obtained from exact perturbation theory (e.g., Bernardeau 1994b), irrespective of the choice of the external tidal term.

Figure 1 shows that the differences between the model predictions are generally small for the spectral indexes $n < 0$, and these are expected to become negligible for decreasing n, approaching the nonsmoothing results ($n = -3$), as obtained previously (Ohta et al. 2003). For $n = -2$ the predictions up to the one-loop order give

$$\sigma^2 \approx \sigma_l^2 + 0.61\sigma_l^4, \quad (86)$$

$$S_3 \approx 3.86 + 3.21\sigma_l^2 \quad (87)$$

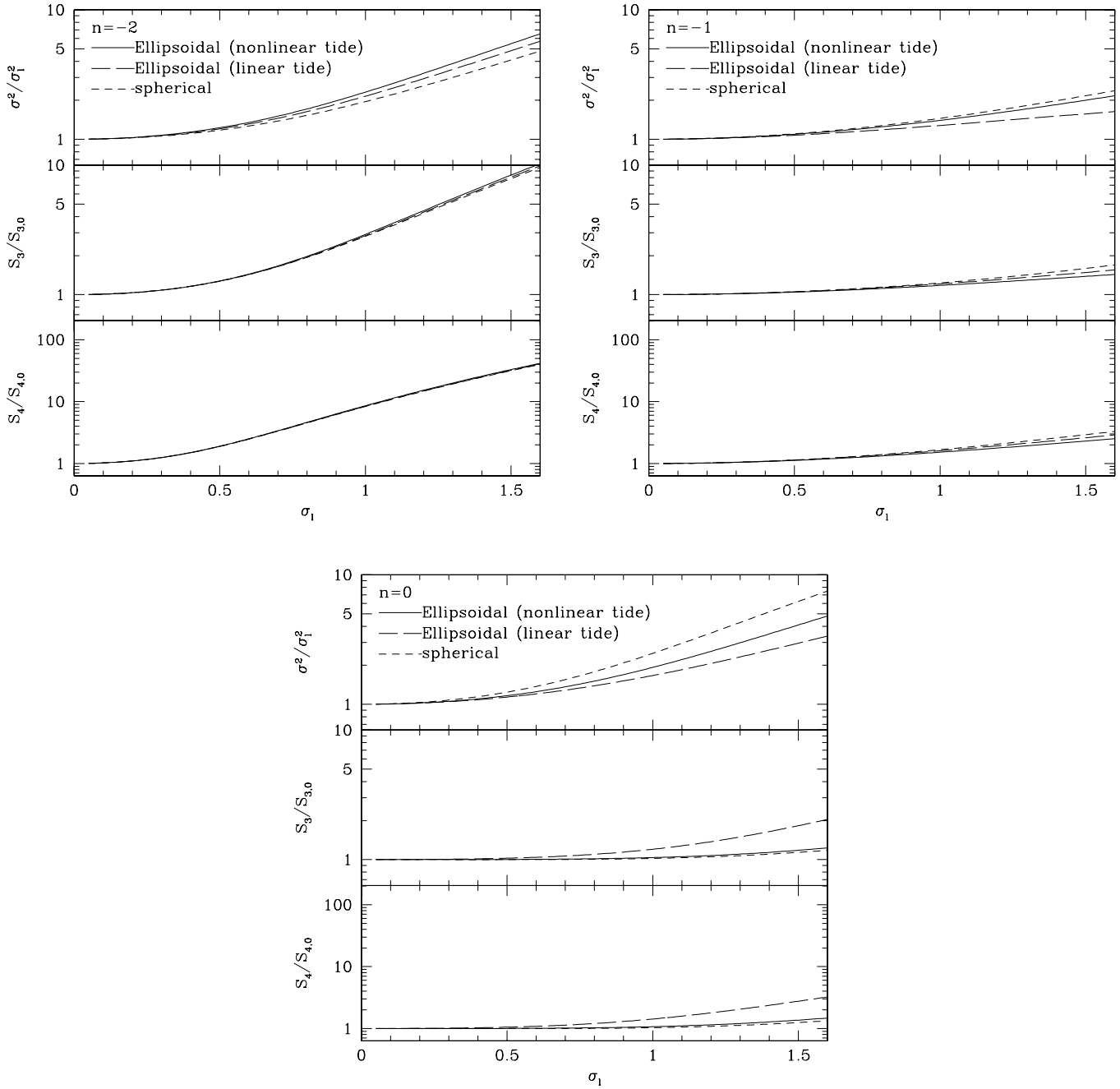

FIG. 1.—Differences between the model predictions for the variance, skewness, and kurtosis. The perturbative results up to the two-loop order are shown in various models of the Lagrangian local dynamics. While the solid and long-dashed lines represent the predictions based on the ECM with nonlinear and linear external tides, respectively, the short-dashed lines indicate the results obtained from the SCM (Fosalba & Gaztañaga 1998a).

for the SCM (Fosalba & Gaztañaga 1998a) and

$$\sigma^2 \approx \sigma_l^2 + 0.88\sigma_l^4, \tag{88}$$

$$S_3 \approx 3.86 + 3.18\sigma_l^2 \tag{89}$$

for exact perturbation theory (Scoccimarro & Frieman 1996; Scoccimarro 1997). Comparing the above results with Table 1, the numerical values of the coefficients are close to those from the ECM prediction. On the other hand, for the $n = 0$ case a large discrepancy appears in the variance σ^2 (Fig. 1). The skewness and the kurtosis also show a relatively large difference. These behaviors are indeed consistent with the PDF shown in Figure 5. The reason why the discrepancy in the model predictions becomes large for increasing n is partially ascribed to the Jacobian in the smoothed density PDF in equation (34). The expression of the Jacobian $|\partial\hat{\lambda}_j/\partial\lambda'_k|$ in equation (36) contains a quantity related to the velocity divergence θ multiplied by the spectral dependence factor, $\gamma/6$. In a previous study of the nonsmoothing case (Ohta et al. 2003), we found that while the differences between the model predictions are almost negligible for the density fields, a large difference appears in the velocity divergence θ. This readily implies that the differences between the model predictions also become significant in the present case, depending on the factor $\gamma = -(n + 3)$. In other words, for a large deviation from $\gamma = 0$, the model predictions sensitively depend on the choice of the Lagrangian local dynamics in the local approximation. That is, not only the evolution of the local density but also the

evolution of the velocity field should be devised to approximate the fluid dynamics precisely. This point is important and should be kept in mind when comparing the predictions with N-body simulations (see § 4.2).

4. COMPARISON WITH N-BODY SIMULATIONS

We are now in a position to discuss the validity and usefulness of the local approximations, comparing the theoretical predictions with N-body simulations. For this purpose, we specifically use the N-body data for scale-free models with initial power spectra $P(k) \propto k^n$ ($n = -2, -1, 0$) (Jing 1998), as well as a CDM model with a cosmological constant (Λ-dominated CDM [ΛCDM]; Jing & Suto 1998). The gravitational force calculation is based on the particle-particle-particle-mesh algorithm. All the models employ $N = 256^3$ dark matter particles in a periodic comoving cube $L_{\rm BOX}^3$, where the box size of the ΛCDM model is chosen as $L_{\rm BOX} = 300\ h^{-1}$ Mpc. While the scale-free models assume an Einstein–de Sitter universe, cosmological parameters of the ΛCDM model are set as $(\Omega_m,\ \Omega_\Lambda,\ h,\ \sigma_8) = (0.3,\ 0.7,\ 0.7,\ 1.0)$, where the normalization σ_8 is the linear rms fluctuation at a top-hat smoothing radius of $R = 8\ h^{-1}$ Mpc. For the scale-free models, the normalization of the density fluctuation is determined by setting the linear rms fluctuation to unity at $R = 0.1 L_{\rm BOX}$. Below, we first present the results for a ΛCDM model (§ 4.1). The PDFs in the scale-free models are compared in § 4.2. In comparing the predictions with simulations, we also present the perturbation results of the local approximation obtained in § 3.

4.1. Λ*CDM Model*

The validity of the local approximation using the SCM has been previously studied by Scherrer & Gaztañaga (2001) in the case of the standard CDM model, and a good agreement with N-body simulation was found. We thus expect the local approximation with both the SCM and the ECM to also provide an excellent agreement with N-body simulation in the case of the ΛCDM model.

Figure 2 shows the PDFs obtained from the N-body data for the top-hat–smoothed density fields (*open squares*). The error bars indicate the 1 σ errors among the three different realizations. The smoothing radii are chosen as $R = 16$, 8, and 2 h^{-1} Mpc (*top to bottom*). In Figure 2 the PDFs from the SCM and the ECM with a linear external tide are depicted as long-dashed and solid lines, respectively. We also calculated the PDFs from the ECM with a nonlinear external tide, but the results are almost the same as obtained from the ECM with a linear external tide. Clearly, these models almost coincide with each other, and the agreement with N-body results is excellent. For comparison, we also plot the empirical model of the lognormal distribution (*short-dashed lines*):

$$P(\delta) = \frac{1}{\sqrt{2\pi}\sigma_{\rm LN}} \frac{1}{1+\delta} \exp\left(-\frac{1}{2\sigma_{\rm LN}^2}\left[\log(1+\delta) + \frac{\sigma_{\rm LN}^2}{2}\right]^2\right), \tag{90}$$

with $\sigma_{\rm LN}^2 = \log(1+\sigma^2)$. Here the quantity σ denotes the variance of the local density field, which is estimated from the N-body simulation. Even given the simplicity of the analytical expression (90), the lognormal PDFs also approximate the N-body results quite accurately. Agreement with N-body simulations still remains good, even at the high-density tails

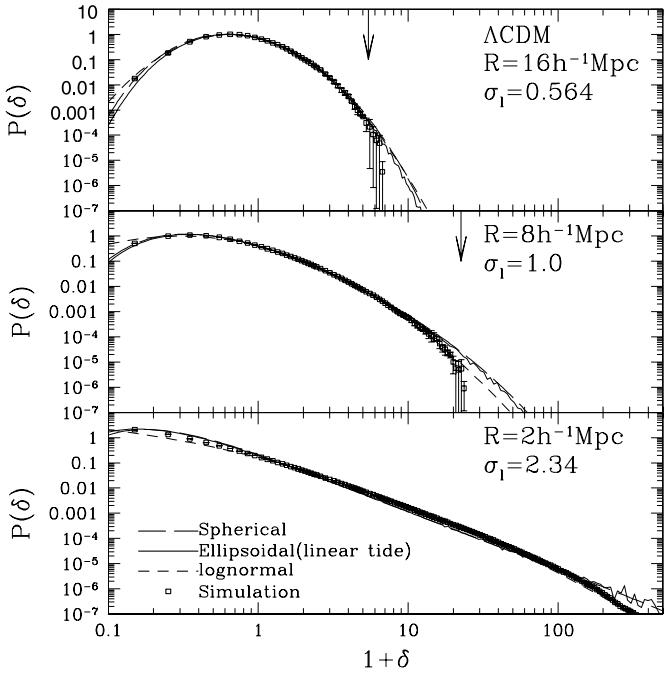

FIG. 2.—PDFs of the density field in the ΛCDM model with a top-hat smoothing window, for $R = 2$ (*bottom*), 8 (*middle*), and 16 h^{-1} Mpc (*top*). The open squares represent the N-body results. The error bars indicate the 1 σ variation among the three different realizations. Values of σ_l in each panel are the linear variance at each smoothing radius. The arrows indicate the mean value of the cutoff density $\delta_{\rm max}$. Note that the cutoff density at $R = 2\ h^{-1}$ Mpc reaches 601. Solid lines show the prediction based on the ECM with a linear external tide. Long-dashed lines show the prediction obtained from the SCM. Short-dashed lines show the lognormal PDF adopting the variance σ^2 calculated directly from the simulations.

of small radii, $R = 2$ and 8 h^{-1} Mpc. Bernardeau & Kofman (1995) discuss the successful lognormal fit of the PDF in the CDM models based on the perturbation results.

In order to check the accuracy of the model predictions, we quantify the cumulants of the density fields. In Figure 3 we plot the variance σ^2, the skewness $S_3 \equiv \langle\delta^3\rangle/\sigma^4$, and the kurtosis $S_4 \equiv (\langle\delta^4\rangle - 3\sigma^4)/\sigma^6$ as functions of smoothing radius (*top to bottom*). In each panel the crosses with error bars indicate the results obtained from the N-body simulations, while the open squares show the results from the local approximation with the ECM, in which the moments $\langle\delta^N\rangle$ are calculated from the full knowledge of the PDF $P(\delta)$ (see eq. [37]). On the other hand, the short-dashed and long-dashed lines show the perturbative calculations of the cumulants based on the ECM up to the one-loop order and two-loop order, respectively (see § 3.2). As a reference, we also plot the leading-order (tree-level) prediction in dotted lines. In contrast to a naive expectation from Figure 2, the ECM prediction based on the PDF significantly deviates from the N-body results at the smaller radius $R \lesssim 8\ h^{-1}$ Mpc, although it roughly matches the perturbation results up to the two-loop order.

Kayo et al. (2001) remarked that the origin of this discrepancy might be due to the fact that the density field δ in N-body simulations does not extend to the entire range between -1 and $+\infty$, but rather is limited in the range $\delta_{\rm min} < \delta < \delta_{\rm max}$, owing to the finite size of the simulation box. Indeed, a closer look at Figure 2 reveals that there exists a sharp cutoff at the high-density tails of the simulated PDFs (*arrows*). To examine the

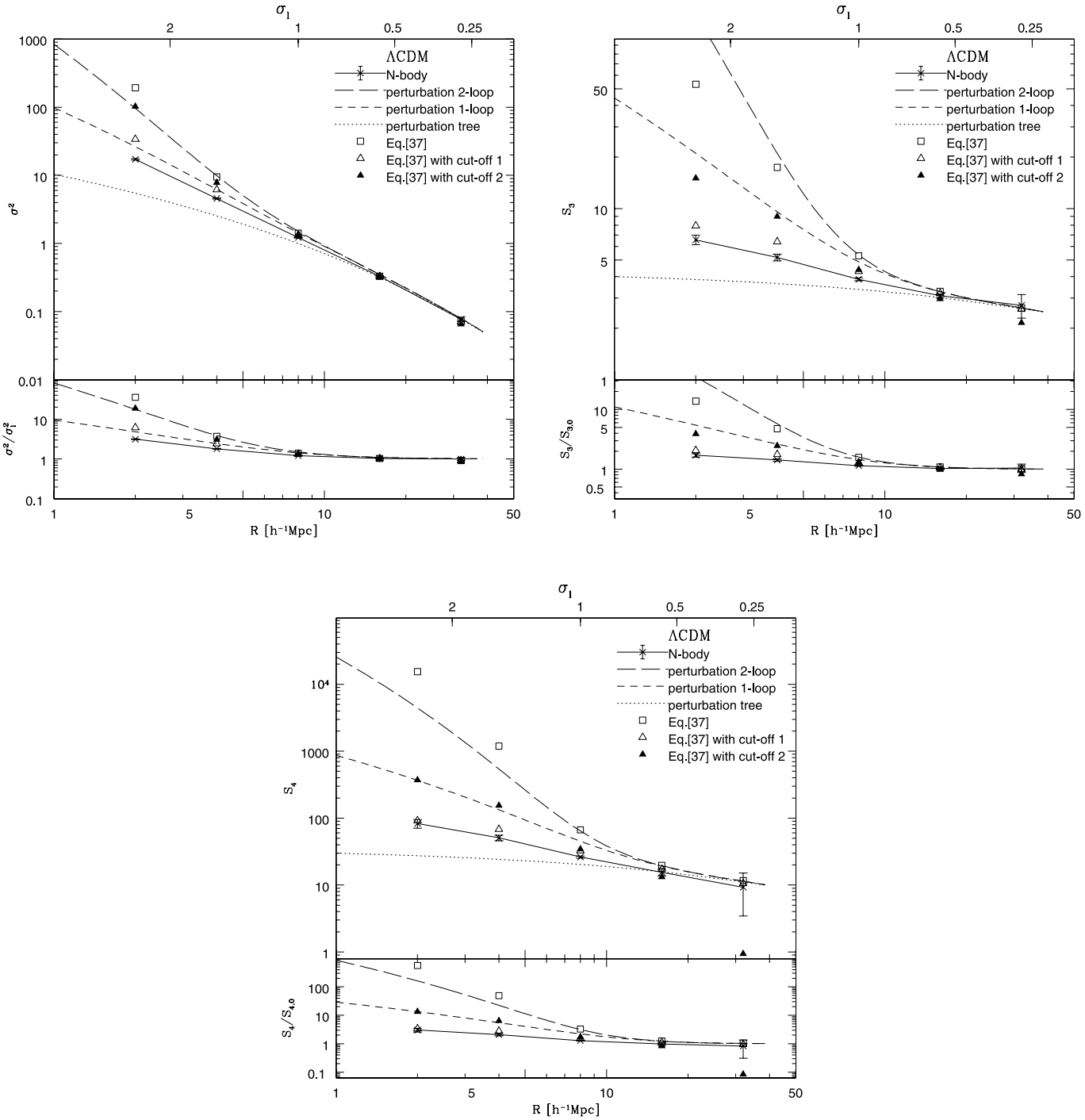

FIG. 3.—Variance (*top left*), skewness (*top right*) and kurtosis (*bottom*) of the density field in the ΛCDM model as functions of smoothing radius R. The crosses with error bars represent the results from N-body simulations. The open squares show the prediction from the ECM with a linear external tide based on a full knowledge of the PDF (eq. [37]). The open (cutoff 1) and filled (cutoff 2) triangles show the same prediction as the open squares but taking into account the limited range of the density PDF, $[\delta_{\rm min}, \delta_{\rm max}]$. While the cutoff values for the open squares are estimated from the N-body data, $\delta_{\rm min}$ and $\delta_{\rm max}$ for the filled triangles are determined from eq. (91) with the help of a theoretical PDF. Long-dashed lines show the perturbative predictions of cumulants based on the ECM up to the two-loop order. Short-dashed lines show the perturbative predictions up to the one-loop order. Dotted lines show the leading-order results of the perturbation theory.

significance of this effect, the ECM predictions of the cumulants taking into account the finite range $[\delta_{\rm min}, \delta_{\rm max}]$ are plotted in Figure 3 (cutoff 1: *open triangles*). The cutoff values $\delta_{\rm min}$ and $\delta_{\rm max}$ are estimated from the N-body data. Furthermore, in Figure 3 we plot the prediction taking into account the cutoff values determined from the simple assumptions that (1) the major effect of the finite range of δ comes from the finite sampling effect and (2) the theoretical PDF is correct if the box size of the simulation becomes infinite. We then have (Kayo et al. 2001)

$$\frac{L_{\rm BOX}^3}{4\pi R^3/3}\int_{-1}^{\delta_{\rm min}} P(\delta)\,d\delta = 1, \quad \frac{L_{\rm BOX}^3}{4\pi R^3/3}\int_{\delta_{\rm max}}^{\infty} P(\delta)\,d\delta = 1, \quad (91)$$

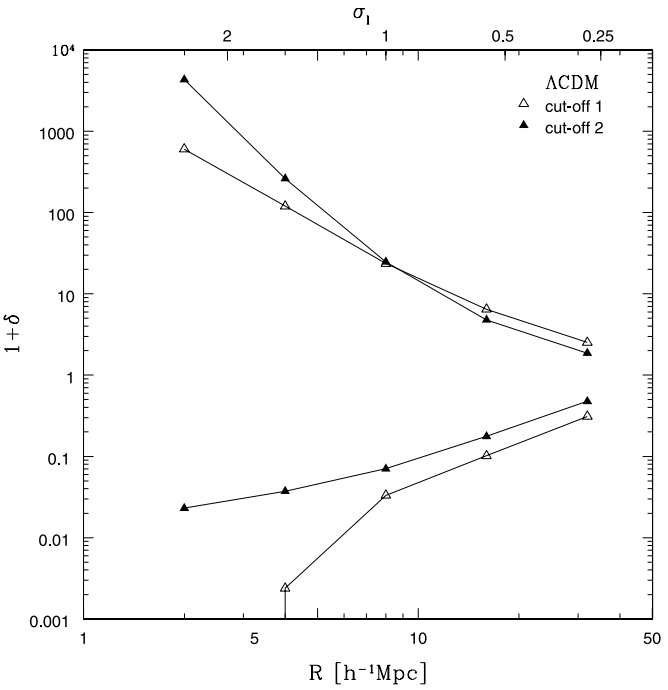

FIG. 4.—Cutoff values $\delta_{\min}$ and $\delta_{\max}$ of the density field as functions of smoothing radii. While the open triangles show the cutoff density estimated from the *N*-body simulations, the filled triangles represent the values obtained from the finite sampling effect (eq. [91]).

where $P(\delta)$ is the PDF obtained from the ECM. The resulting cutoff values ($\delta_{\min}$, $\delta_{\max}$) are plotted as functions of smoothing radii in Figure 4.

The resulting amplitudes of the cumulants are significantly reduced, and the model prediction turns out to reproduce the simulation data very well in the case using the *N*-body data (cutoff 1). This readily implies that the apparent discrepancy in the cumulants mainly comes from the limited range of the density in the PDF, and one concludes that the local approximation with the ECM provides an accurate prediction for both the density PDF and the cumulants in the ΛCDM model. Similarly, one expects the accuracy of the model prediction to still remain good for the local approximation with the SCM. Note, however, that the predictions with equation (91) still exhibit a discrepancy at smaller scales, $R \lesssim 4\ h^{-1}$ Mpc. This means that the finite sampling effect might be a major numerical effect from the limited range of the density, but there still remain other nonnegligibile effects. The discreteness effect could be an important source for the discrepancy on small scales. This point is particularly important for the self-consistent calculation of cumulants and should be treated carefully. Keeping these remarks in mind, we next proceed to the scale-free models.

4.2. *Scale-free Models*

N-body simulations in a scale-free model with index $n \leq -1$ generally suffer from spurious numerical effects compared to the CDM case, which significantly affects the statistical properties of the mass distribution (e.g., Colombi et al. 1996). This is not exceptional in our case. Figure 5 shows the density PDFs for $n = -2$ to 0 models at different smoothing radii; $R = 0.15L_{\rm BOX}$, $0.1L_{\rm BOX}$, and $0.02L_{\rm BOX}$. For larger smoothing radii, the PDF obtained from the simulations (*open squares*) has a sharp cutoff at high-density tails. Because of this, the amplitude of the cumulants is significantly reduced, and the *N*-body simulation fails to reproduce even the leading-order results of perturbation theory (see Figs. 6 and 7). Nevertheless, focusing on the moderately non-Gaussian tails of the PDF, we find that the predictions based on the SCM and ECM show a good agreement with *N*-body simulations for smaller spectral indexes, $n = -2$ and -1. Especially at the nonlinear scale ($R = 0.02L_{\rm BOX}$), the PDF from the ECM seems to improve the prediction compared to the results obtained from the SCM. This is even true for the spectral index $n = 0$, indicating that the ECM provides a more physical model of Lagrangian local dynamics than the SCM. Interestingly, the lognormal model also provides a good approximation to the *N*-body simulations, irrespective of the nature of the initial spectra and the smoothing scales. Apparently, this contradicts the perturbation results, which predict a strong spectral dependence in the weakly nonlinear regime (Bernardeau 1994b). As stated by Bernardeau (1994a) and Bernardeau & Kofman (1995), however, the perturbation results themselves resemble the lognormal PDF near the index $n = -1$. Furthermore, a systematic comparison with the lognormal prediction done by Kayo et al. (2001), who basically used the same *N*-body data as ours, shows that the lognormal model prediction tends to deviate from the simulation for $n = 0$ and $+1$ in the weakly nonlinear regime, even if the cutoff of the PDF is taken into account. Thus, no serious contradiction is found, at least for the quality of our data.

Now consider the cumulants of the density fields. Figures 6 and 7 show the variance, the skewness, and the kurtosis, which are compared with the predictions from the SCM and the ECM, respectively. As anticipated from Figure 5, the amplitudes of the cumulants from *N*-body data are significantly reduced, and the local approximation without cutoff (*open squares*) generally overpredicts the simulation results. A more serious aspect is that the simulation does not converge to the tree-level results of perturbation theory. Even the predictions up to the one-loop correction overpredict the simulation results. As previously remarked by Colombi et al. (1996), the recovery of tree-level results is difficult because of the limited size of the *N*-body simulations, and care must be taken in order to correct the spurious numerical effects. Colombi et al. (1996) devised a correction to the finite volume effect to explore the scaling properties of the PDFs. Nevertheless, the general tendency for our simulations and those obtained by Colombi et al. (1996) is quite similar, i.e., the nonlinear corrections to the skewness and the kurtosis seen in the *N*-body results are generally small, and their amplitudes are nearly scale-independent.

In Figures 6 and 7, repeating the same procedure as in the ΛCDM case, we plot the cumulant predictions from the PDF taking into account the cutoff (cutoff 1: *open triangles*; cutoff 2: *filled triangles*). Then, the overall behaviors of the model predictions seem to be greatly improved. The agreement between the model prediction and the *N*-body simulation is reasonably good in both the cutoff 1 and cutoff 2 cases, except for the strongly nonlinear regime, $\sigma_l \gtrsim 5$. A closer look at these figures shows that the prediction based on the ECM provides a better approximation than that of the SCM, especially for the $n = 0$ case. Note, however, that most of the predictions for the variance slightly overpredict the simulation, except for the $n = -2$ case. The overprediction might be partially ascribed to the cutoff of the density [$\delta_{\min}$, $\delta_{\max}$], since the width of the PDF quantified by the variance sensitively depends on the cutoff. On the other hand, the reduced

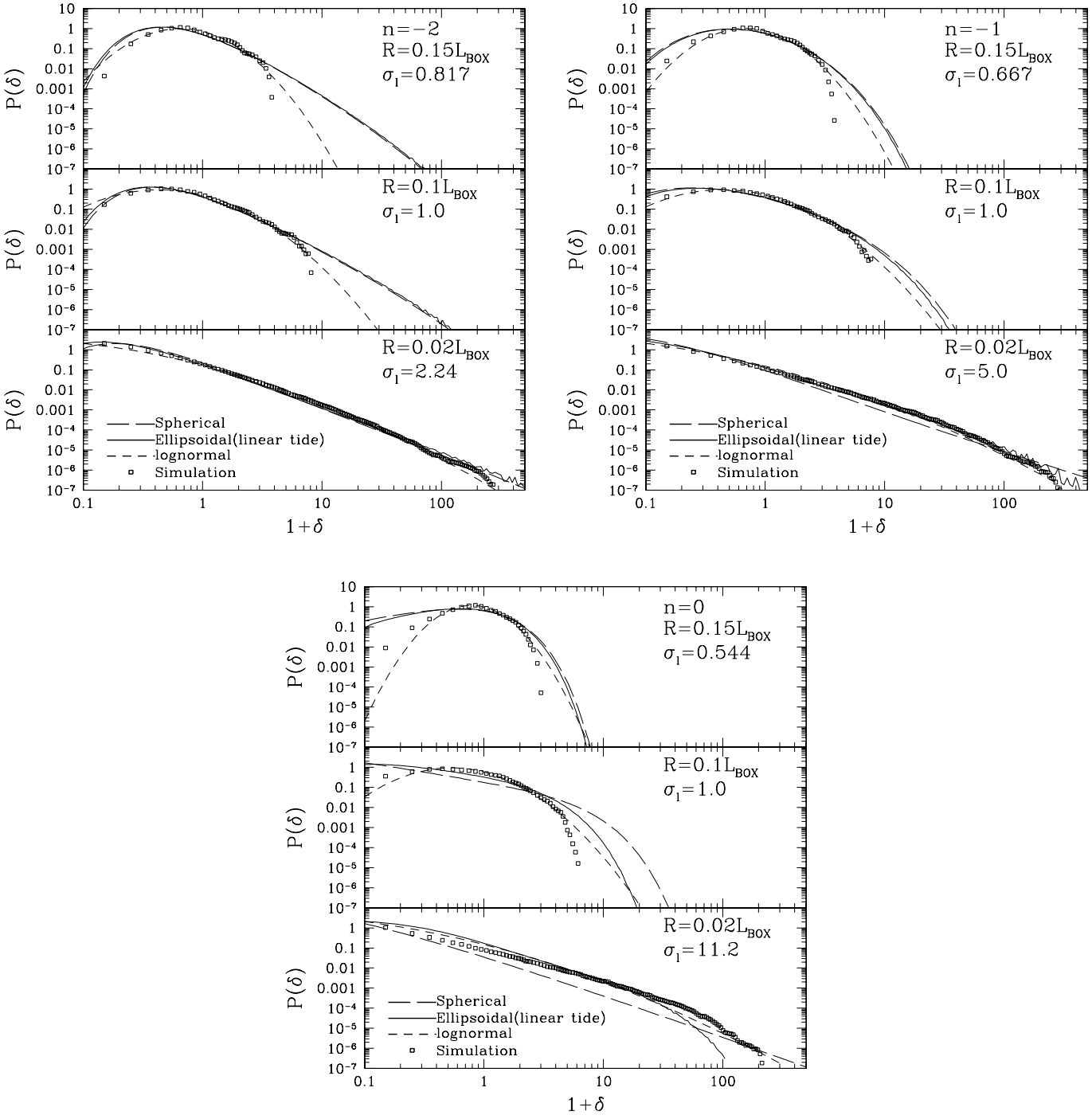

FIG. 5.—Same as Fig. 2 but with scale-free models ($n = -2$, -1, and 0) for $R = 0.02L_{\rm BOX}$ (*bottom*), $0.05L_{\rm BOX}$ (*middle*), and $0.15L_{\rm BOX}$ (*top*).

amplitudes S_3 and S_4 rather characterize the shape of the PDF, which could be, in principle, less sensitive to the cutoff of the high-density tails than the cumulants themselves if the tails of the PDF converge closely enough to zero. Actually, the shape of the predicted PDF resembles that of the PDF in the simulations, as in Figure 5. The same tendency has been previously reported by Fosalba & Gaztañaga (1998a).

Thus, at the level of quality of the *N*-body data, the local approximation with both the SCM and the ECM works reasonably well, and the approximation with the ECM even slightly improves the prediction. Of course, one must still care about the cutoff density arising from spurious numerical effects. In this respect, the validity of the local approximation may just reach an acceptable level. In addition, another important caveat is drawn from the strong model dependence of the predictions. As discussed in § 3.3, the local approximation itself becomes more sensitive to the choice of the Lagrangian local dynamics as the deviation from the spectral index $n = -3$ gets larger. This is clearly seen in the strong model dependence of the one-point PDF (Fig. 5) and the nonlinear correction for the cumulant prediction (Fig. 1). Furthermore, recall the fact that the linear variance σ_l scales as $\sigma_l \propto R^{-(n+3)/2}$. This means that a slight decrease of the smoothing radius R significantly increases the linear variance on nonlinear scales, $\sigma_l \gtrsim 1$. Hence, one expects the model prediction for $n \geq 0$ to suffer from the nonlinear corrections more seriously,

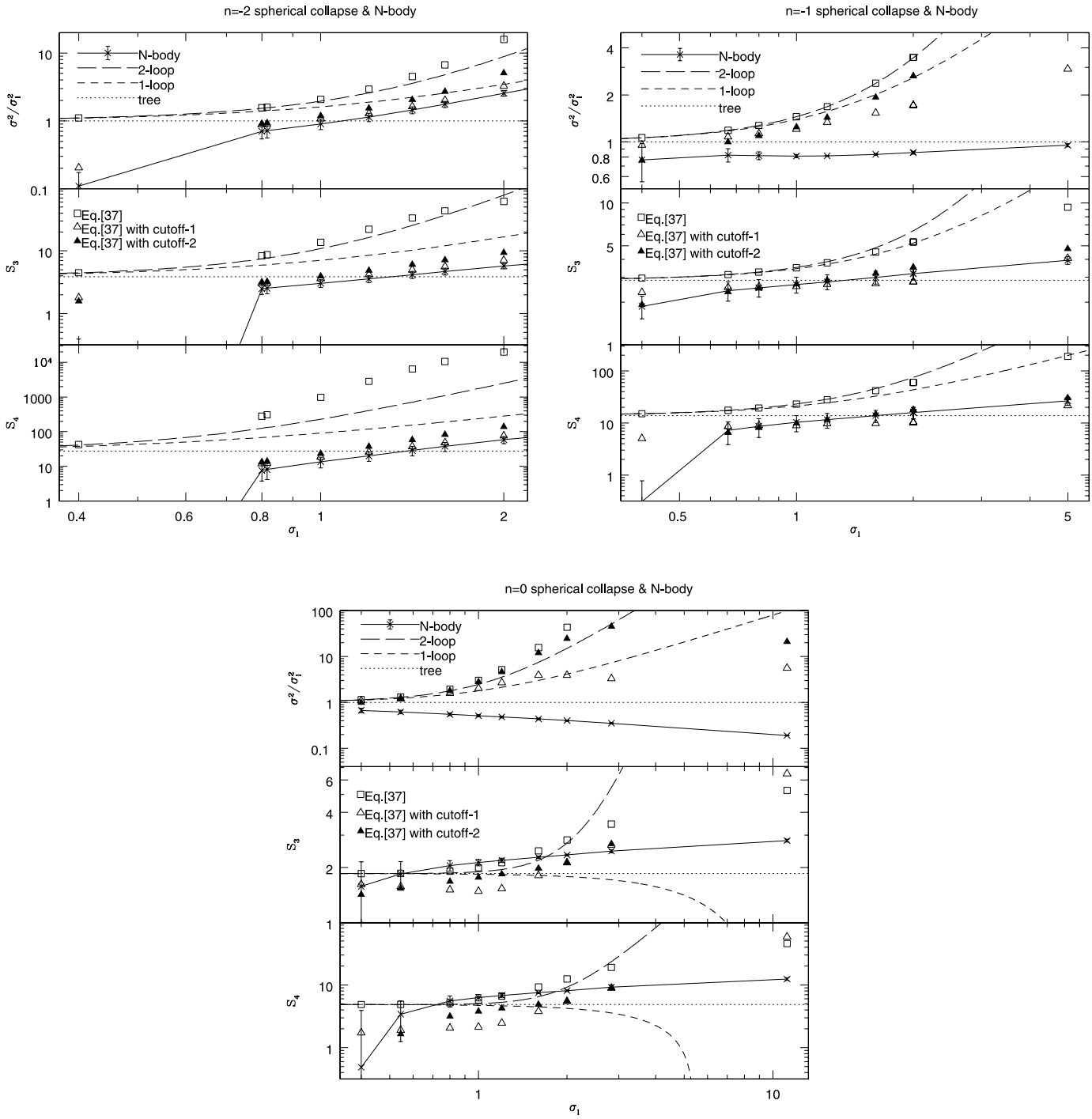

FIG. 6.—Variance, skewness, and kurtosis of the *N*-body results in scale-free models, compared with the SCM predictions. The crosses with error bars and the solid line represent the *N*-body simulations. The squares show the predictions from the SCM based on a full knowledge of the PDF (eq. [37]). The open (cutoff 1) and filled (cutoff 2) triangles are the same as the squares, but we take into account the cutoff of the density field. While the long-dashed lines represent the perturbative predictions up to the two-loop order, the short-dashed lines indicate the results up to the one-loop order. As a reference, we also plot the leading-order results of perturbation theory in dotted lines.

compared to the initial spectra with $n = -2$ or -1 or ΛCDM. Therefore, the local approximation with the ECM should be used with caution for the index $n \geq 0$.

5. CONCLUSION AND DISCUSSION

In the present paper we critically examined the validity and the usefulness of the local approximation to the PDF and the cumulant predictions. Adopting the ellipsoidal and the spherical collapse models as representative models of the Lagrangian local dynamics, the PDFs and the cumulants are calculated taking into account the smoothing effect, and the resulting predictions are compared with the *N*-body simulations with Gaussian initial conditions. Because of the cutoff of the density arising from spurious numerical effects, a detailed comparison in cumulants becomes difficult, and a correction for the cutoff density should be self-consistently incorporated into the model prediction. At the level of quality of the *N*-body data, however, the local approximations with both the SCM and ECM successfully reproduce the *N*-body results for the PDFs and the cumulants, although the

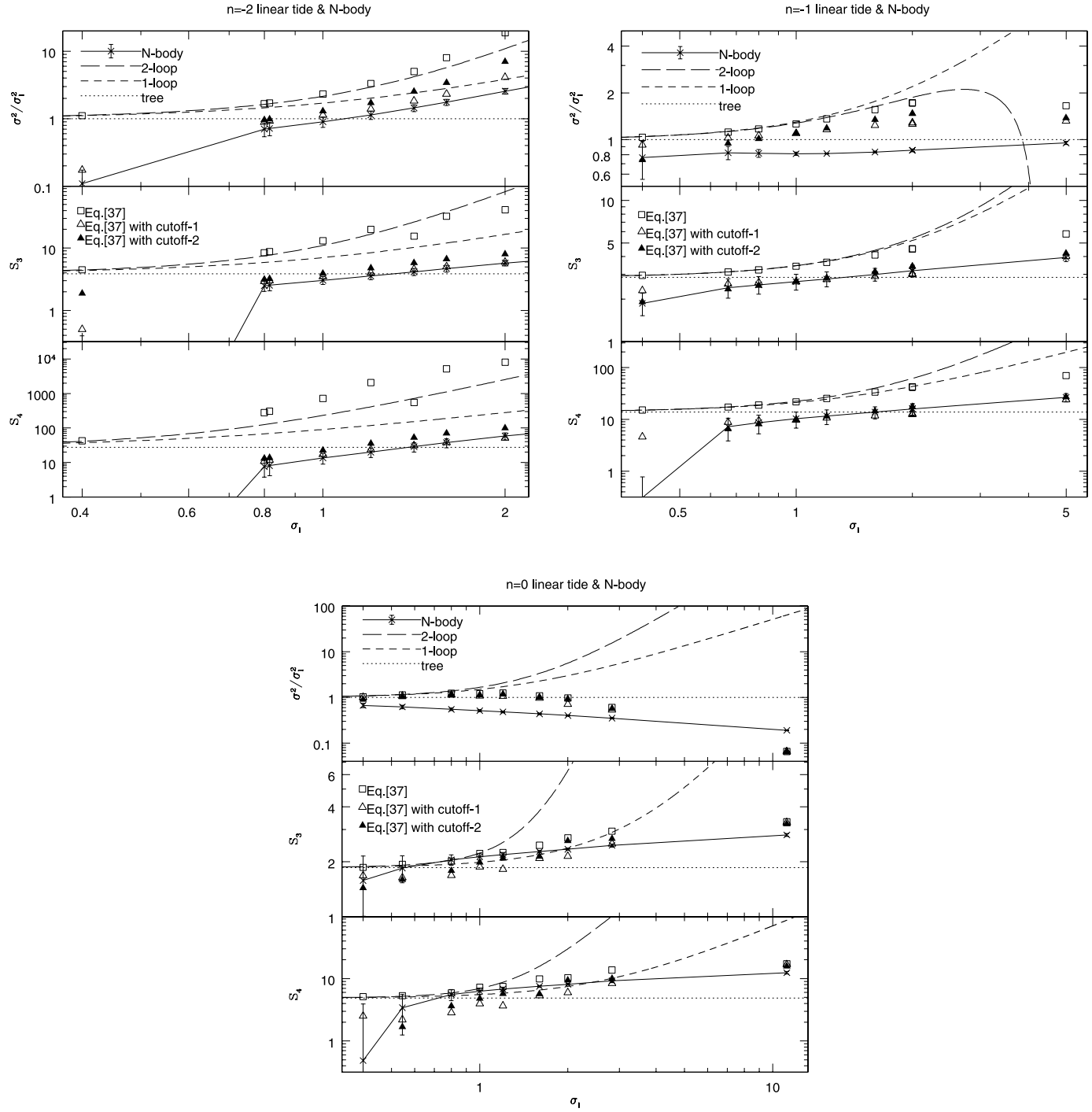

FIG. 7.—Same as Fig. 6 but for theoretical predictions based on the ECM with a linear external tide approximation.

self-consistent calculation of the local approximation presented in this paper (cutoff 2) still needs to be improved. This is indeed the case of the ΛCDM model and scale-free models with indexes $n = -2$ and -1. For a scale-free model with $n = 0$, while the discrepancy between the model prediction and the simulation result is manifest in the local approximation with the SCM, the agreement with *N*-body results still remains good for the ECM prediction. A detailed discussion reveals that the prediction based on the local approximation sensitively depends on the slope of the initial spectrum and that the predictions for $n > 0$ become more sensitive to the nonlinear dynamics of the local collapse model. Thus, a more delicate modeling of the Lagrangian local dynamics is required for an accurate prediction. Taking this point carefully, we therefore conclude that the local approximations with the SCM and ECM provide excellent approximations to the *N*-body simulations for CDM and scale-free models with $n < 0$ in both the linear and the nonlinear regimes, $0 \lesssim \sigma_l \lesssim 5$, while the local approximation should be used with caution in the $n \geq 0$ cases.

In this paper we found that the predictions based on the ECM somewhat improve the approximation; however, the degree of improvement is not very large as long as a CDM-like initial spectrum (i.e., effective spectral index $n_{\rm eff} = -3 - d\log\sigma_l^2/d\log R < 0$) is involved. Compared to the

prediction from the SCM, the calculation of the PDF from the ECM is rather complicated and requires a time-consuming numerical integration. It seems that the SCM provides a simpler prescription for the PDF in real space and is practically more useful than the ECM. However, if one considers the one-point statistics in redshift space, the situation might be changed drastically. As reported by Scherrer & Gaztañaga (2001), the local approximation with the SCM only provides a good approximation to the redshift-space PDFs when $\sigma_l \lesssim 0.4$. A part of this reason is ascribed to the fact that the model prediction cannot recover the linear perturbation result, referred to as the Kaiser effect (Kaiser 1987); the variance in the redshift space σ_z^2 is related to the one in the real space as

$$\sigma_z^2 = \left(1 + \frac{2}{3}f_\Omega + \frac{1}{5}f_\Omega^2\right)\sigma_l^2. \tag{92}$$

In contrast to the SCM, which leads to the incorrect prediction $\sigma_z^2 = (1 + f_\Omega/3)^2\sigma_l^2$, the Kaiser effect in equation (92) can be correctly recovered by means of the ECM. The derivation of equation (92) is presented in the Appendix. This fact is very interesting and also provides the important suggestion that the nonsphericity of the Lagrangian local dynamics plays a crucial role in computing the one-point statistics in redshift space and is indeed essential for an accurate prediction. A detailed analysis of the model predictions in redshift space is now in progress and will be described elsewhere.

We thank the referee, E. Gaztañaga, for many useful comments and suggestions for improving the original manuscript. We also thank Y. P. Jing for kindly providing us his *N*-body data and Y. Suto for comments and discussions. I. K. acknowledges support from a Takenaka-Ikueikai Fellowship. This work is supported in part by a grant-in-aid for Scientific Research from the Japan Society for the Promotion of Science (14740157).

APPENDIX

DERIVATION OF THE KAISER FACTOR BY THE ELLIPSOIDAL COLLAPSE MODEL

In this appendix we derive the Kaiser effect (eq. [92]) from the ECM. Assuming the distant-observer approximation, let us consider the local density located at $\boldsymbol{r} = (r_1,\ r_2,\ r_3)$ in real space and choose the third axis as the line-of-sight direction. Denoting the corresponding coordinate in redshift space by $\boldsymbol{s} = (s_1,\ s_2,\ s_3)$, the relation between $\boldsymbol{r}$ and $\boldsymbol{s}$ becomes

$$s_1 = r_1, \qquad s_2 = r_2, \qquad s_3 = r_3 + v_3/H, \tag{A1}$$

where v_3 is the line-of-sight component of the peculiar velocity field. Then the local density in redshift space, ρ_s, can be expressed in terms of the quantities in real space as

$$\rho_s = \frac{dM}{ds_1\, ds_2\, ds_3} = \frac{dM}{dr_1\, dr_2\, dr_3[1 + (1/H)(\partial v_3/\partial r_3)]} = \frac{\rho}{1 + (1/H)(\partial v_3/\partial r_3)}. \tag{A2}$$

The peculiar velocity field at the position $\boldsymbol{r}$ is described by the motion of the homogeneous ellipsoid. Introducing a new coordinate along the principal axis of the ellipsoid, $\boldsymbol{r}' = (r_1',\ r_2',\ r_3')$, the peculiar velocity v is given by

$$v_i = \bar{v}_i + \left(\frac{\dot{\alpha}_i}{\alpha_i} - H\right)r_i' \tag{A3}$$

in the new coordinate system. Here $\bar{v}_i$ is the bulk velocity of the ellipsoid. The new coordinate $\boldsymbol{r}'$ does not necessarily coincide with the original one, $\boldsymbol{r}$. Rather, it is related to the original coordinate through the Euler angle, i.e., $\boldsymbol{r}' = R_3(\psi)R_2(\theta)R_3(\phi)\boldsymbol{r}$, where R_i is the rotational matrix with respect to the ith axis. Using this fact, the quantity in equation (A3) is transformed into the original frame, and we obtain

$$\begin{aligned}\frac{\partial v_3}{\partial r_3} &= \sum_{i=1}^{3}[R_3(\psi)R_2(\theta)R_3(\phi)]_{3i}^{-1}\left(\frac{\dot{\alpha}_i}{\alpha_i} - H\right)[R_3(\psi)R_2(\theta)R_3(\phi)]_{i3} \\ &= \left(\frac{\dot{\alpha}_1}{\alpha_1} - H\right)\cos^2\psi\sin^2\theta + \left(\frac{\dot{\alpha}_2}{\alpha_2} - H\right)\sin^2\psi\sin^2\theta + \left(\frac{\dot{\alpha}_3}{\alpha_3} - H\right)\cos^2\theta.\end{aligned} \tag{A4}$$

Here we neglect the bulk velocity. Substituting the above into equation (A2) yields

$$1 + \delta_s = \frac{1 + \delta}{(1/H)\left[(\dot{\alpha}_1/\alpha_1)\cos^2\psi\sin^2\theta + (\dot{\alpha}_2/\alpha_2)\sin^2\psi\sin^2\theta + (\dot{\alpha}_3/\alpha_3)\cos^2\theta\right]}, \tag{A5}$$

where the quantity δ_s is the density fluctuation in redshift space. Note that the expression is exact under the distant-observer limit. In the linear perturbation, the quantity α_i in equation (A5) is replaced with $a(1 - \lambda_i)$ (eq. [19]). We have

$$\delta_s = \delta_l + f_\Omega\left(\lambda_1\cos^2\psi\sin^2\theta + \lambda_2\sin^2\psi\sin^2\theta + \lambda_3\cos^2\theta\right), \tag{A6}$$

where $f_\Omega \equiv d\ln D/d\ln a \simeq \Omega_m^{0.6}$. Hence, the linear variance in redshift space, σ_z^2, is expressed as

$$\sigma_z^2 \equiv \langle \delta_s^2 \rangle = \left(1+\frac{2}{3}f_\Omega\right)\left\langle (\lambda_1+\lambda_2+\lambda_3)^2 \right\rangle + \frac{1}{15}f_\Omega^2 \langle 3\left(\lambda_1^2+\lambda_2^2+\lambda_3^2\right) + 2(\lambda_1\lambda_2+\lambda_2\lambda_3+\lambda_3\lambda_1)\rangle, \tag{A7}$$

where we have taken averages over the angles ψ, θ, and ϕ. Finally, the ensemble averages over the variable λ_i are taken with a knowledge of the distribution function in equation (21):

$$\sigma_z^2 = \left(1+\frac{2}{3}f_\Omega+\frac{1}{5}f_\Omega^2\right)\sigma_l^2. \tag{A8}$$

This is exactly the Kaiser effect. Note that in cases adopting the SCM, the variable λ_i is $\delta_l/3$. Hence, the ensemble average over δ_l in equation (A7) immediately yields an incorrect prediction, $\sigma_z^2 = (1+f_\Omega/3)^2\sigma_l^2$.

REFERENCES

Bernardeau, F. 1992, ApJ, 392, 1
———. 1994a, A&A, 291, 697
———. 1994b, ApJ, 433, 1
Bernardeau, F., & Kofman, L. 1995, ApJ, 443, 479
Bond, J. R., & Myers, S. T. 1996, ApJS, 103, 1
Coles, P., & Jones, B. 1991, MNRAS, 248, 1
Coles, P., Melott, A. L., & Shandarin, S. F. 1993, MNRAS, 260, 765
Colombi, S., Bouchet, F. R., & Hernquist, L. 1996, ApJ, 465, 14
Doroshkevich, A. G. 1970, Astrofiz., 6, 581
Fosalba, P., & Gaztañaga, E. 1998a, MNRAS, 301, 503
———. 1998b, MNRAS, 301, 535
Gaztañaga, E., & Yokoyama, J. 1993, ApJ, 403, 450
Hamilton, A. J. S. 1985, ApJ, 292, L35
Jing, Y. P. 1998, ApJ, 503, L9
Jing, Y. P., & Suto, Y. 1998, ApJ, 494, L5
Kaiser, N. 1987, MNRAS, 227, 1
Kayo, I., Taruya, A., & Suto, Y. 2001, ApJ, 561, 22
Nakamura, T. T., & Suto, Y. 1995, ApJ, 447, L65
Ohta, Y., Kayo, I., & Taruya, A. 2003, ApJ, 589, 1
Saslaw, W. C., & Hamilton, A. J. S. 1984, ApJ, 276, 13
Scherrer, R. J., & Gaztañaga, E. 2001, MNRAS, 328, 257
Scoccimarro, R. 1997, ApJ, 487, 1
Scoccimarro, R., & Frieman, J. A. 1996, ApJ, 473, 620
Taruya, A., Hamana, T., & Kayo, I. 2003, MNRAS, 339, 495
Taylor, A. N., & Watts, P. I. R. 2000, MNRAS, 314, 92
Ueda, H., & Yokoyama, J. 1996, MNRAS, 280, 754